ResearchGate

See discussions, stats, and author profiles for this publication at: https://www.researchgate.net/publication/321386063

Mascon Models for Small Body Gravity Fields

Conference Paper · August 2017

CITATIONS
10

READS
1,316

2 authors:

Ryan P. Russell
University of Texas at Austin
187 PUBLICATIONS **3,127** CITATIONS

SEE PROFILE

Patrick T. Wittick
University of Texas at Austin
4 PUBLICATIONS **24** CITATIONS

SEE PROFILE

All content following this page was uploaded by Ryan P. Russell on 30 November 2017.

The user has requested enhancement of the downloaded file.

AAS 17-743

MASCON MODELS FOR SMALL BODY GRAVITY FIELDS

Patrick T. Wittick[*], **Ryan P. Russell**[†]

In the context of small bodies, mascon models can be attractive because they are simple to compute, implement, and parallelize. However, to achieve a reasonable surface accuracy, mascon models typically require too many elements to be competitive with other models. Here, mascon models are revisited, with the intent to minimize the number of elements, optimize the placement of the elements, and modify the base model of elements in order to improve computational efficiency, while enabling their use at low altitudes. The use of spherical harmonics elements, buried within a mascon model, is shown to offer model evaluation speedups and reduced memory footprints at little or no accuracy cost over homogeneous mascon models. The resulting mixed element models expand the design space for optimal packing structures while providing fast, accurate field evaluations to enable rapid small body trajectory searches.

INTRODUCTION

Interest in and the development of missions to the solar system's numerous small bodies has rapidly accelerated in recent years. With operational missions like OSIRIS-REx[1] and Dawn,[2] planned missions like Psyche,[3] and private industry interest in asteroid resource mining and utilization, there is a clear need for flexible mission design tools well-suited to the small body environment. In particular, the ability to perform rapid explorations of the trajectory design space is invaluable during early studies of mission concepts and mid-mission trajectory re-planning. Looking toward future generations of spacecraft navigation tools, autonomous onboard algorithms stand to benefit from efficient gravity field implementations. In this paper, a new small body gravitational model is presented that facilitates rapid trajectory design by leveraging the fast field evaluations offered by mascon and spherical harmonics methods while maintaining much of the accuracy and global validity of higher-fidelity polyhedral models.

When modeling the gravity field of an irregularly-shaped small body, the polyhedral method provides a particularly convenient and robust solution.[4] Under a constant density assumption, the potential evaluation can be converted from a volume integral to a surface integral over the facets and edges of a finite-element (FEM) polyhedral shape model. This feature makes the polyhedral method consistent with the FEM shape models often used in the mission planning process. However, since every potential evaluation requires a summation over every facet and edge of the shape model, this method can be computationally inefficient and unsuitable for the needs of rapid trajectory design.

Like polyhedral shape models, spherical harmonics[5] are useful in the representation of both the topography and the gravity field of a small body; in fact, the gravitational spherical harmonics may be directly derived from the topographic harmonics.[6] A similar calculation may be performed to find the spherical harmonic coefficients for a constant density polyhedron.[7] However, the classical application of this method suffers from two major weaknesses in the context of small celestial bodies: 1) the potential field diverges inside the Brillouin sphere of the body, and; 2) the series representation of the potential requires an excessive number of terms for highly non-spherical bodies. Recently, work by Takahashi, et al.[8] and Casotto and Casotto[9]

[*] Graduate Research Assistant, Department of Aerospace Engineering and Engineering Mechanics, The University of Texas at Austin, 210 E. 24th St., Austin, TX.
[†] Associate Professor, Department of Aerospace Engineering and Engineering Mechanics, The University of Texas at Austin, 210 E. 24th St., Austin, TX.

has sought to address the former problem by introducing and advancing *interior* spherical harmonics fields. These fields, in contrast to *exterior* spherical harmonics fields, are located outside a shape model and have a region of convergence that lies completely within the interior field's reference sphere. These interior harmonics expansions are quite useful when estimating a localized field near the body surface, but a theoretically infinite number of these expansions must be generated to represent the field over the entire body surface simultaneously. Another approach uses ellipsoidal harmonics, which have a region of convergence that lies exterior to a reference ellipsoid.[10] Since the shapes of many small bodies are more closely approximated by ellipsoids rather than spheres, ellipsoidal harmonics offers convergence advantages over spherical harmonics expansions in the small body domain.

Gravity field interpolation schemes offer a particularly fast means of obtaining field evaluations, but that speed comes at the cost of long upfront calculations and large memory requirements.[11–13] In addition to memory and speed, interpolation methods often trade smoothness, continuity, and exactness (i.e. the force model may not be a solution to Laplace's equation). Interpolation methods have been applied at both planetary and small celestial bodies.

Mascon models have heritage as a means of representing localized gravitational anomalies.[14–19] In the 1970s, mascon models gained popularity as an alternative to spherical harmonics when estimating the gravity fields of the Earth and the Moon, especially when attempting gravity field inversion with sparse satellite orbit determination data.[14–18] Typically mascons were applied as a single surface layer overlaying an oblate spheroid and used to represent small deviations from that underlying model. This technique has continued more recently at Ganymede using Galileo flyby data.[19] More significantly, surface mascon models have been utilized with the GRACE mission as a means of representing equivalent water height over the Earth's surface at high resolution.[20,21] Other work has demonstrated that, when measurements of a high-degree and -order spherical harmonics field are used as observations in a least-squares gravity field inversion problem, the Earth's gravity field may be represented at high fidelity by an oblate spheroid and a buried layer of mascons.[22]

Mascon models are particularly suited to small bodies due to their ability to model irregular shapes and density distributions at arbitrary resolution.[23] While the mascon approach provides a good approximation of the far-field environment, the discretized mass distribution results in degraded potential evaluations near the mascon elements. The recent work by Tardivel, where several different mascon packing schemes were evaluated for their accuracy, demonstrated the drawbacks inherent in a constant density mascon model for a small body.[24] Pearl and Hitt have employed interior and surface meshes for use in an alternative mascon method,[25–27] while Hesar et al. leveraged multiple interior spherical harmonics expansions to model density variations within an asteroid.[28]

The goal of the current effort revisits the development of mascon models at small bodies with the goal of providing simple, fast, and accurate gravity evaluations over a global exterior domain. The gravity modeling tool resulting this work, dubbed the Multiple Mascon and Exterior Spherical Harmonics (MultiMESH) model, is designed to suit a broad range of small bodies of interest. It employs a flexible shape model packing method, which is controlled by the user and guided by a small body's geometry, to represent the body with a set of discrete, spherical elements. These elements are then assigned either point-mass or spherical harmonic models based on their size and location. Once the geometry is fixed, a batch least-squares estimator solves for the gravitational parameters and/or spherical harmonics coefficients of the elements using measurements of the body's polyhedral potential. This process imbues the set of discrete elements with higher-fidelity information than other methods, while maintaining the efficiency of uniform mascon and spherical harmonic models. Additionally, since any and all spherical harmonics elements within the model are constrained beneath the shape model surface, the model has no issues with divergence and is globally valid.

MULTIPLE MASCON AND EXTERNAL SPHERICAL HARMONICS MODEL

In this section, an overview of the construction and evaluation of the MultiMESH model is given. Special emphasis is given to the flexible shape model packing tool that supports the gravity model, as the discrete-element arrangements it yields have a significant impact on the performance of the fully-constructed model. The gravitational potential and acceleration equations for the MultiMESH model are then developed.

Table 1: Descriptions of Common Packing Arrangements

Type	Name	Symbol	Description
I	Uniform	$\bullet$	Small elements of a uniform size are densely packed on a precomputed in/out grid throughout the inside of the shape model.
II	Multiple-Layer Uniform	x	Multiple layers of uniformly-packed elements, potentially varying in size across layer boundaries.
III	Multiple-Core	$\square$	Geometrically simple arrangment of several large mass elements placed in the largest spaces available.
IV	Core-Shell	$*$	A pairing of Multiple-Core and Multi-Layer Uniform packing; one or more large "core" elements are placed within an inner layer, then enveloped within uniform smaller elements in an outer shell layer.
V	Infilled Multiple-Core	$\triangle$	Large elements packed first as in Type III. Remaining spaces inside the shape model are "infilled" with smaller mascons.

Element Packing Techniques

The MultiMESH model is underpinned by a flexible and broadly applicable discretized-element packing method. In the context of small bodies, "packing" is the process of determining how the interior space of a body will be discretized. For this work, the packing process arranges a combination of point-mass and spherical harmonics elements within a small body shape model in such a way that the overall gravity model evaluation time for a given error threshold is minimized. Note that elements which are assigned spherical harmonics expansions are most often those herein referred to as "core" elements, though this association is not required for either the estimation procedure or in evaluations of the force model.

The shape model packing trade space is defined by three axes: how the location of each element is determined, the size and shape of the valid element placement domain, and the size of each element. For the packing geometry, all elements are assumed to be constant-density spheres. However, their gravity signature can be altered by adjusting the mass or supplemented with spherical harmonics, as discussed in later sections.

Some techniques used by Tardivel to place mass elements are adapted for the current work.[24] The first technique requires a three-dimensional grid placed around and through a body shape model, the nodes of which are defined to be "in" or "out" of the shape model. The in/out status of each node can be predetermined by calculating the solid angle subtended by the shape model about the node. Shape models subtend a solid angle of 4π about interior points and less than 4π about exterior points. Elements may be centered at the "in" nodes and spaced so that they do not overlap given a user-defined element radius. The second technique does not require an in/out grid; instead, the element is placed at a user-defined starting location within the shape model, then shifted automatically by small distances to find a location at which its radius is maximized. The direction of each shift is defined to be opposite the direction of the closest shape model vertex. This shifting is performed repeatedly until some tolerance on the change in element radius is met. Tardivel used the second technique to place a single large element, but it has been adapted for this work to place multiple elements in the same fashion. Implicit in these element placement techniques is determination of the element radius. For the first technique, the radius is defined by the user ahead of the packing procedure, while element sizing is automatic when using the second technique. The two techniques may be combined by automatically placing elements within the largest spaces inside the shape model, then surrounding those elements with uniform smaller elements attached to the remaining interior grid points.

Controlling the valid spatial domain for the elements is as simple as scaling the vertex positions of the shape model to the desired size. A reduced-scale shape model may be used to place elements near the core of the body or create a shell closer to the surface; all that is required is a recomputation of the in/out grid. Repeatedly scaling the shape model enables the generation of multi-layered packing schemes. In this context, a "layer" is a region of space contained entirely within the full-scale shape model that is bounded externally

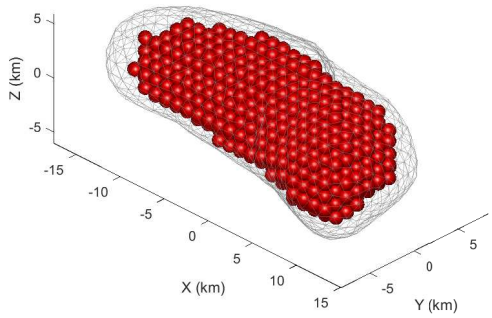

(a) Uniform

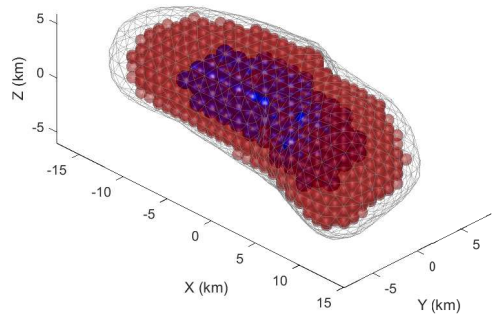

(b) Multiple-Layer Uniform

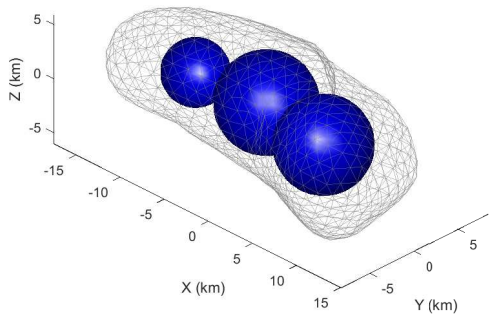

(c) Multiple-Core

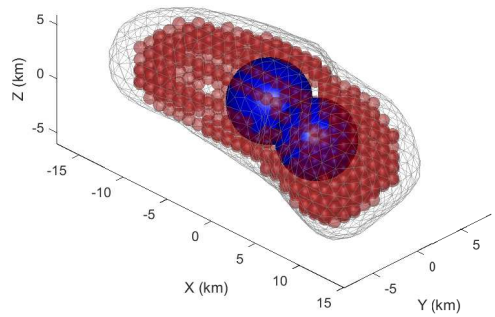

(d) Core-Shell

Figure 1: Shape model for 433 Eros packed with example cases for the first four packing arrangements in Table 1. The schemes in (a) and (c) are packed inside an 85% scale shape model, while the scheme in (b) consists of two layers within 60% and 90% scale shape models, and the scheme in (d) consists of two layers within 70% and 85% scale shape models. All subfigures show a full-scale 1708-facet Eros shape model for reference.

by a smaller-scaled shape model, and internally bounded either by the origin or an even smaller shape model. The advantages of such layering are clear. We may define layers to exist somewhat below the shape model surface in order to reduce the errors due to field irregularities generated by the point-mass singularities near the surface. Additionally, layering allows us to place larger elements near the core of the body, which can reduce the overall number of elements in the model without significantly reducing accuracy at or near the body surface.

The three packing techniques, in combination with layering, can be used to generate a large number of varied packed-element schemes. Generally, these schemes fall into five categories: Uniform, Multiple-Layer Uniform, Multiple-Core, Core-Shell, and Infilled Multiple-Core packing. See Table 1 for summaries of these structures. Examples of the first four packing scheme types are given for 433 Eros in Figure 1, while an example of an Infilled Multiple-Core scheme at the asteroid 216 Kleopatra is shown in Figure 2. Kleopatra, as a well-known contact binary, lends itself naturally to a structure containing two large core elements at either end of the hambone shape.

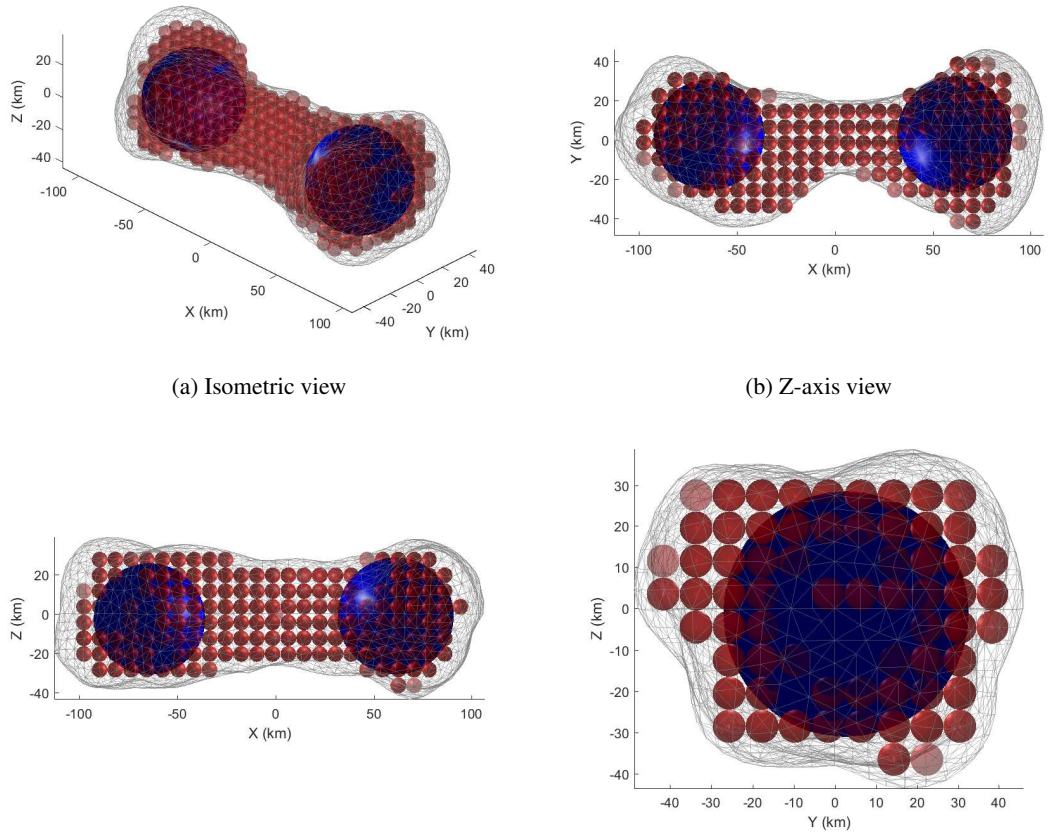

(a) Isometric view

(b) Z-axis view

(c) Y-axis view

(d) X-axis view

Figure 2: Shape model for 216 Kleopatra[29] (217 x 94 x 81 km) packed with an Infilled Multiple-Core (Type V) element packing structure. This low-resolution, single-layer representation is packed within a 90% shape model. The small elements are 8 km in diameter, while the large cores are about 56.8 km and 59.6 km in diameter.

Potential and Force Model

Since the MultiMESH model incorporates mascons and exterior spherical harmonics expansions into its force model, it is key to detail how the gravity fields of these elements combine. The classic Legendre form of spherical harmonics series suffers from singularities at the poles and the use of computationally expensive trigonometric functions. Instead, a Cartesian approach known as Pines' Method is employed here.[30] Before presenting the expression for the potential, it is necessary to express the components of the unit vector in the direction of the relative position of the measurement point and denote them s_{ik}, t_{ik}, u_{ik}.

$$\begin{aligned} r_{ik} &= \sqrt{x_{ik}^2 + y_{ik}^2 + z_{ik}^2} \\ s_{ik} &= x_{ik}/r_{ik} \\ t_{ik} &= y_{ik}/r_{ik} \\ u_{ik} &= z_{ik}/r_{ik} \end{aligned} \tag{1}$$

Using these components of the radial unit vector, the gravitational potential due to the ith body at the kth

evaluation point may be written:

$$U_{P,ik} = \frac{\mu_i}{r_{ik}}\left[1 + \sum_{n=0}^{\infty}\left(\frac{r_{a,i}}{r_{ik}}\right)^n \sum_{m=0}^{n} A_{n,m}(u_{ik})\Big\{C^i_{n,m}\rho_m(s_{ik},t_{ik}) + S^i_{n,m}\iota_m(s_{ik},t_{ik})\Big\}\right]. \tag{2}$$

where μ_i is the gravitational parameter of the attracting body, r_{ik} is the radial distance of the kth evaluation point relative to the center of mass of the attracting body, $r_{a,i}$ is the radius of the Brillouin sphere for the attracting body, $A_{n,m}$ is related to the Legendre polynomial of degree n, $\rho_m(s_{ik},t_{ik})$, and $\iota_m(s_{ik},t_{ik})$ are recursively defined, position-dependent quantities, and $C^i_{n,m}$ and $S^i_{n,m}$ are the spherical harmonics coefficients of the ith attracting body. The integers n and m may be limited to a maximum degree and order if an approximation of the full spherical harmonics potential is desired. The recursion relationships for $A_{n,m}$, $\rho_m(s_{ik},t_{ik})$, and $\iota_m(s_{ik},t_{ik})$ are given as

$$A_{n+1,m+1}(u_{ik}) = (n+1+m)A_{n,m} + u_{ik}A_{n,m+1} \tag{3}$$

$$\begin{aligned}\rho_m(s_{ik},t_{ik}) &= \mathrm{Re}\{(s_{ik}+t_{ik}\sqrt{-1})^m\} = s_{ik}\rho_{m-1}(s_{ik},t_{ik}) - t_{ik}\iota_{m-1}(s_{ik},t_{ik})\\ \iota_m(s_{ik},t_{ik}) &= \mathrm{Im}\{(s_{ik}+t_{ik}\sqrt{-1})^m\} = s_{ik}\iota_{m-1}(s_{ik},t_{ik}) + t_{ik}\rho_{m-1}(s_{ik},t_{ik})\end{aligned} \tag{4}$$

Before arriving at the total potential expression, the equation for gravitational potential due to a point-mass must be added. The well-known expression for the gravitational potential $U_{MC,jk}$ due to the jth mascon at the kth evaluation point is

$$U_{MC,jk} = \frac{\mu_j}{r_{jk}}, \tag{5}$$

where μ_j is the gravitational parameter of the jth mascon and r_{jk} is the radial distance from the point mass to the evaluation point. If a given body is represented by N mascons and M spherical harmonics elements, the component potential fields may be superposed to yield the total gravitational potential $U_{\text{MESH},k}$ at the kth evaluation point:

$$U_{\text{MESH},k} = \sum_{i=1}^{M} U_{P,ik} + \sum_{j=1}^{N} U_{MC,jk}. \tag{6}$$

Since the terms in each summation in Eq. (6) may be computed independently, the opportunities for parallelization when performing potential evaluations are obvious. We can express the total gravitational acceleration vector, $\ddot{\mathbf{R}}_k$, at the same point by taking the gradient of the potential:

$$\ddot{\mathbf{R}}_{\text{MESH},k} = \sum_{i=1}^{M} \nabla U_{P,ik} + \sum_{j=1}^{N}\Big(-\frac{\mu_j}{r^3_{jk}}\mathbf{r_{jk}}\Big), \tag{7}$$

where the acceleration due to the ith spherical harmonics element is

$$\nabla U_{P,ik} = \ddot{\mathbf{r}}_{ik} = a_1\hat{\mathbf{i}} + a_2\hat{\mathbf{j}} + a_3\hat{\mathbf{k}} + a_4\frac{\mathbf{r}_{ik}}{r_{ik}} \tag{8}$$

with the coefficients defined by

$$
\begin{aligned}
a_1 &= \sum_{n=0}^{\infty} \frac{r_{a,i}^n \mu_i}{r_{ik}^{n+2}} \sum_{m=0}^{n} A_{n,m}(u_{ik}) m E_{n,m} \\
a_2 &= \sum_{n=0}^{\infty} \frac{r_{a,i}^n \mu_i}{r_{ik}^{n+2}} \sum_{m=0}^{n} A_{n,m}(u_{ik}) m F_{n,m} \\
a_3 &= \sum_{n=0}^{\infty} \frac{r_{a,i}^n \mu_i}{r_{ik}^{n+2}} \sum_{m=0}^{n} A_{n,m+1}(u_{ik}) D_{n,m} \\
a_4 &= \sum_{n=0}^{\infty} \frac{r_{a,i}^n \mu_i}{r_{ik}^{n+2}} \sum_{m=0}^{n} [(n+1+m) A_{n,m}(u_{ik}) + u_{ik} A_{n,m+1}(u_{ik})] D_{n,m}
\end{aligned}
\tag{9}
$$

The reader is referred to Pines' original work for full definitions of the recursive quantities $E_{n,m}$, $F_{n,m}$, and $D_{n,m}$. For this work, a Fortran implementation of Pines' method is employed.

ESTIMATION OF MODEL PARAMETERS

The simplest option when designing a mascon model is to assign a constant bulk density to each of the mascon elements.[24] Recent work has shown that acceleration measurements collected from flybys at small bodies can be used to estimate both mascon- and spherical harmonics-based gravity model parameters.[8,23] Additionally, Russell and Arora demonstrated that measurements of a high-degree and -order spherical harmonics field for the Earth may be used in a batch least squares estimation problem to estimate the masses of a buried spherical array of mascons.[22] A similar technique, outlined here, has now been extended to the small body problem for the MultiMESH model.

For this application, estimates of the gravitational parameters (μ) of all elements present in the model as well as the coefficients ($C_{n,m}$ and $S_{n,m}$) of any spherical harmonics elements in the model are sought. To ensure numerical stability in the estimation procedure, normalized spherical harmonics coefficients are used. These normalized forms are

$$
\begin{aligned}
\overline{C}_{n,m} &= \mathcal{A}_{n,m} C_{n,m} \\
\overline{S}_{n,m} &= \mathcal{A}_{n,m} S_{n,m}
\end{aligned}
\tag{10}
$$

where $\mathcal{A}_{n,m}$ is a normalization factor given by

$$
\mathcal{A}_{n,m} = \sqrt{\frac{(n+m)!}{(2-\delta_{0,m})(2n+1)(n-m)!}} \tag{11}
$$

To ensure the potential does not change due to this normalization, the associated Legendre polynomials are normalized by the inverse of $\mathcal{A}_{n,m}$ in the Legendre form of the potential.

The measurement model is drawn from Eq. (6) since the estimation process fits the MultiMESH potential to the polyhedral potential. If estimates of only the gravitational parameters of the elements are sought, the measurement model and the estimation problem are linear. The same applies if estimates of only the spherical harmonics coefficients are sought. However, if the estimated state vector contains both gravitational parameters and spherical harmonics coefficients, the problem becomes nonlinear because the observation-state partial derivatives depend on components of the state vector. Therefore, a nonlinear batch least squares estimator is used to estimate all model parameters simultaneously. In cases where the estimated state consists only of either gravitational parameters or spherical harmonics coefficients, the nonlinear estimation problem reduces to a linear one, and the filter converges after one iteration. Choosing values of the polyhedral potential as truth measurements, the nonlinear measurement model for this estimation problem may be formulated as

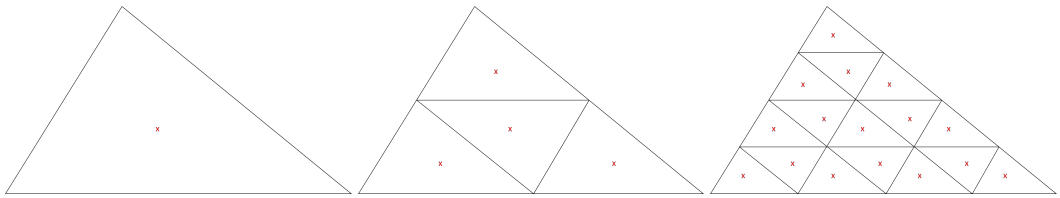

(a) $\alpha = 0$ (b) $\alpha = 1$ (c) $\alpha = 2$

Figure 3: An example of triangular facet bisection for $\alpha = 0, 1$, and 2. The "x" marks represent the centroid locations for this facet.

$$\mathbf{z} = \mathbf{h}(\mathbf{x}) + \epsilon, \quad \mathbf{z} = \begin{bmatrix} U_{\text{poly},1} \\ \vdots \\ U_{\text{poly},k} \\ \vdots \\ U_{\text{poly},l} \end{bmatrix}, \quad \mathbf{h}(\mathbf{x}) = \begin{bmatrix} U_{\text{MESH},1} \\ \vdots \\ U_{\text{MESH},k} \\ \vdots \\ U_{\text{MESH},l} \end{bmatrix}, \quad \epsilon \sim \mathcal{N}(\mathbf{0}, \mathbf{R}) \tag{12}$$

The state vector $\mathbf{x}$ may contain both gravitational parameters and normalized spherical harmonics coefficients. Measurement vector $\mathbf{z}$ contains l polyhedral potential measurements $U_{\text{poly},k}$ which are taken one meter above the centroids of the shape model facets to maximize the observability of the system. The observation-state relationship $\mathbf{h}(\mathbf{x})$ consists of l MultiMESH gravitational potential values given by the state vector $\mathbf{x}$, taken at the same locations as the values in $\mathbf{z}$. The observation error vector ϵ also has length l, but its components are zero since perfect knowledge of the polyhedral truth field is assumed.

For the least-squares problem to be observable, at least as many measurements as states are required. However, it may be desirable to design models containing so many elements that more potential measurements than the number of shape model facets will be required. In this case, a simple triangular facet bisection method is used to obtain 4^α measurement points per facet, where α is the number of bisections performed. The bisection method works by subdividing each triangular facet into four similar triangles by connecting the midpoints of each side. The bisection can be performed recursively α times, and the projected centroids of the subdivided triangles are then taken as new measurement points. Using the centroids to define measurement points prevents clustering along the edges of the facets and ensures a more uniform spatial distribution of measurements. Figure 3 shows how splitting a single triangular facet affects the number and locations of measurements on that facet.

We seek to minimize a performance index

$$J(\mathbf{x}) = (\mathbf{z} - \mathbf{h}(\mathbf{x}))^T \mathbf{R}^{-1} (\mathbf{z} - \mathbf{h}(\mathbf{x})), \tag{13}$$

for which the nonlinear normal equations for a batch estimator are

$$\begin{gathered} (\mathcal{H}^T \mathbf{R}^{-1} \mathcal{H} + \mathbf{P}_{\mathbf{xx}}^{-1}) \Delta \hat{\mathbf{x}} = \mathcal{H}^T \mathbf{R}^{-1} \Delta \mathbf{z} + \mathbf{P}_{\mathbf{xx}}^{-1} \Delta \overline{\mathbf{x}} \\ \Delta \mathbf{z} = \mathbf{z} - \mathbf{h}(\mathbf{x}^*) \end{gathered} \tag{14}$$

when *a priori* information $\mathbf{x}_0^* \sim \mathcal{N}(\overline{\mathbf{x}}_0, \mathbf{P}_{\mathbf{xx}})$ is included as an observation of the state. Taking $\mathbf{x}^*$ to represent the reference state vector, we have for the observation-state partials

$$\mathcal{H} = \frac{\partial \mathbf{h}(\mathbf{x})}{\partial \mathbf{x}} \Big|_{\mathbf{x}=\mathbf{x}^*} \tag{15}$$

To obtain the state estimate, we loop over Eq. (14), updating the state deviations and $\mathcal{H}$ each iteration:

$$\begin{aligned} \mathbf{x}^* &\leftarrow \mathbf{x}^* + \Delta\hat{\mathbf{x}} \\ \Delta\overline{\mathbf{x}} &\leftarrow \Delta\overline{\mathbf{x}} - \Delta\hat{\mathbf{x}} \end{aligned} \tag{16}$$

Convergence of the filter is determined by comparing the Euclidean norm of the state deviation vector $\Delta\hat{\mathbf{x}}$ against a convergence tolerance of 10^{-7} after each iteration. Choosing as the *a priori* state a constant density mascon solution with any spherical harmonics coefficients set to zero leads to convergence for all the packing scenarios tested.

It is important to note that the gravity inversion problem is typically ill-conditioned due to poor observability, particularly when attempting to estimate the mass parameters of a dense mascon distribution.[31,32] In practical terms, the ill conditioning is physical, as multiple distributions can lead to the same gravity signature. Since this work is primarily focused on generating models to perform fast and accurate field evaluations, not on estimating internal density distributions, physically improbable mascon distributions (i.e. extreme mass discontinuities in neighboring mascons) may result. The success of the MultiMESH model in this work is judged by how closely the model configurations match the exterior gravity field of the polyhedron, and how well they trade off memory and computational speed with traditional models when performing field evaluations. Relating the estimated model parameters to the internal density distribution of a small body using the MultiMESH model is an attractive area of future work.

RESULTS

The aforementioned packing and parameter estimation procedures are used to sample the design space and find optimal model archetypes which yield advantageous tradeoffs of memory, speed, and accuracy when compared to dense mascon, spherical harmonic, and polyhedral models. This section begins by defining the model performance metrics, then moves on to use those parameters in the evaluation of model performance and the search for Pareto frontiers in the design trade-space. Finally, a specific comparison case is discussed which pointedly demonstrates the benefits of the methods developed in this paper.

All error metrics are given relative to a high-fidelity gravity field of asteroid 433 Eros, calculated from a 10152-facet polyhedral shape model.[33] Eros was chosen for these experiments due to its elongated and irregular shape and the availability of data related to the body, obtained from the NEAR mission and Earth-based observation. All physical distances from here forward are normalized by the reference radius of Eros, $R_a = 16$ km.

Nomenclature

The packing and estimation algorithms described to this point enable the generation of a wide variety of gravity models. For development, comparison, and application, it is important to develop a shorthand naming scheme which permits the uniqe identification of a particular model. The nomenclature presented here takes the form of a modular, alphanumeric identification code, and it encapsulates information about the number, type, distribution, and physical extent of the discrete elements in a particular model.

Since each layer of elements tends to be relatively homogeneous, it makes sense to construct the model ID code from a concatenation of layer identification codes. Using rough pseudocode for character string assignment, a model ID code begins with the innermost layer and ends with the outermost one:

<model_ID>= <innerlayer_ID>_<layer2_ID>_....._<outerlayer_ID>

Each layer code then contains relevant information about the elements present in that layer. Generally, each layer code is structured such that:

<layer_ID>= <elementType><number_of_this_type>_<layer_bounds><elementSize>

The term "elementType" refers to either mascons ("M") or spherical harmonics ("SH"), while "elementSize" is either the uniform radius of the mascons in this layer expressed as a fraction of the body reference

radius or the degree and order of any spherical harmonics elements in this layer. Layer bounds are expressed as a pair of two digit integers representing the scale factors of the shape model bounds (e.g. 40-70 for a layer extending from a 40% scaled shape model to one scaled to 70% of full size). So, for instance, a core layer containing 3 spherical harmonics elements within a 60% shape model, where the spherical harmonics field sizes are 10x10, 12x12, and 15x15, can be represented with the code:

<layer1_ID>= SH3_00-60_10.12.15

Suppose instead there were a layer of 1028 mascons between 60% and 90% scale shape models, each having a normalized radius of 0.02. The code for this layer would then be:

<layer2_ID>= M1028_60-90r0.02

If a model were to consist of these two layers, placed on top of one another, their layer ID codes could be concatenated to form a single code for the entire model.

<model_ID>= SH3_00-60_10.12.15_M1028_60-90r0.02

This scheme can be used to describe any packing structure of Types I through IV (as listed in Table 1). Since Type V structures combine spherical harmonics elements and mascons in a single layer, they require a slightly different layer ID code. The code still follows the layer ID template above, but the layer bounds are mentioned only once in the usual position for a mascon layer. A modifier "C" is also placed before the "M" to indicate that the mascons are *combined* with the spherical harmonics elements in the same layer. For example, consider a layer extending from the origin to the bounds of an 80% scale shape model, containing 2 spherical harmonics elements (field sizes 15x15 and 10x10) and 554 mascons of normalized radius 0.025. The code for such a layer would be:

<hybridlayer_ID>= SH2_10.15_CM554_00-80r0.025

This slightly different scheme can still be combined with other layer codes to form model codes, as above. This nomenclature is used in the following section to identify the models tested in order to reduce the exposition required to describe each model.

Performance Metrics

Measurements of the root mean square (RMS) and maximum absolute acceleration error magnitude are used as metrics for model accuracy in this work. Suppose that Q evenly-distributed measurements of the gravitational acceleration vector are taken per discrete altitude interval. Then, using the polyhedral truth model and the MultiMESH model in question, the acceleration vectors $\ddot{\mathbf{r}}_{\text{poly}}$ and $\ddot{\mathbf{r}}_{\text{MESH}}$, respectively, may be found at each measurement point. The RMS acceleration error at the tested altitude is then

$$\xi_{\text{RMS}} = \sqrt{\frac{\sum_{k=1}^{Q} |\ddot{\mathbf{r}}_{\text{poly},k} - \ddot{\mathbf{r}}_{\text{MESH},k}|^2}{Q}} \tag{17}$$

The maximum error is recorded at each altitude as well:

$$\xi_{\text{max}} = \max_{k} |\ddot{\mathbf{r}}_{\text{poly},k} - \ddot{\mathbf{r}}_{\text{MESH},k}| \tag{18}$$

Computational speed for a given model is measured directly and reported below in milliseconds. The runtimes given are averages over 42500 acceleration evaluations taken at 425 evenly-spaced vertices of the shape model, projected outward to 100 discrete altitudes. The MultiMESH model uses a Fortran implementation, and is compiled using the Intel®Fortran Compiler 17.0 and run on an Intel®Xeon®E5-1650 v3 CPU at 3.50GHz. Memory requirements are measured by the minimum number of quantities that must be stored in memory to provide field evaluations. Each mascon requires the storage of a position vector (3 components) and the gravitational parameter (μ), while each spherical harmonics element requires a position vector for its center, μ, reference radius r_a, and $n_{\text{max}}^2 + 2n_{\text{max}}$ coefficients, where n_{max} is the maximum degree of the spherical harmonics element (assuming the degree and order of the element's expansion are equivalent). If

we denote η as the total number of memory locations required by a given model containing N mascons and M spherical harmonics elements, then

$$\eta = 4N + 5M + \sum_{i=1}^{M} (n_{\max,i}^2 + 2n_{\max,i}) \tag{19}$$

Polyhedral models require the storage of all vertex positions (3 floating point numbers per vertex) and an integer mapping matrix (3 integers per face) to relate the vertices to the model facets. Taking into account that integers occupy half the memory of floating point numbers, the equivalent number of floating points that must be stored for the polyhedral truth model (10152 facets, 5078 vertices) is 30462. For a lower fidelity, 1708 facet shape model, the number of required memory locations is 5130.

MultiMESH Model Performance

A selection of 36 MultiMESH models are generated using the packing schemes in Table 1. The models have elements layered and buried at varying depths beneath the 433 Eros shape model surface. Acceleration errors are evaluated against the polyhedral truth model for altitudes from 0 R_a to 0.3125 R_a above the shape model surface. Altitude at a given point is reckoned along the radial vector from the origin, and is defined to be the distance between the shape model surface and the point in question along that vector. The altitude domain is partitioned in two regions, one from the surface to 0.15625 R_a and the other from 0.15625 R_a to 0.3125 R_a. Much of the lower region falls within the Brillouin sphere, while the outer region contains a mixture of points both interior and exterior to the Brillouin sphere. Each model is represented by a single point in each plot, and each point is labeled according to the corresponding model number in Table 2. Lower resolution polyhedral models with 7790 facets and 1708 facets are included with diamond markers ($\diamond$) for comparison with the MultiMESH models.

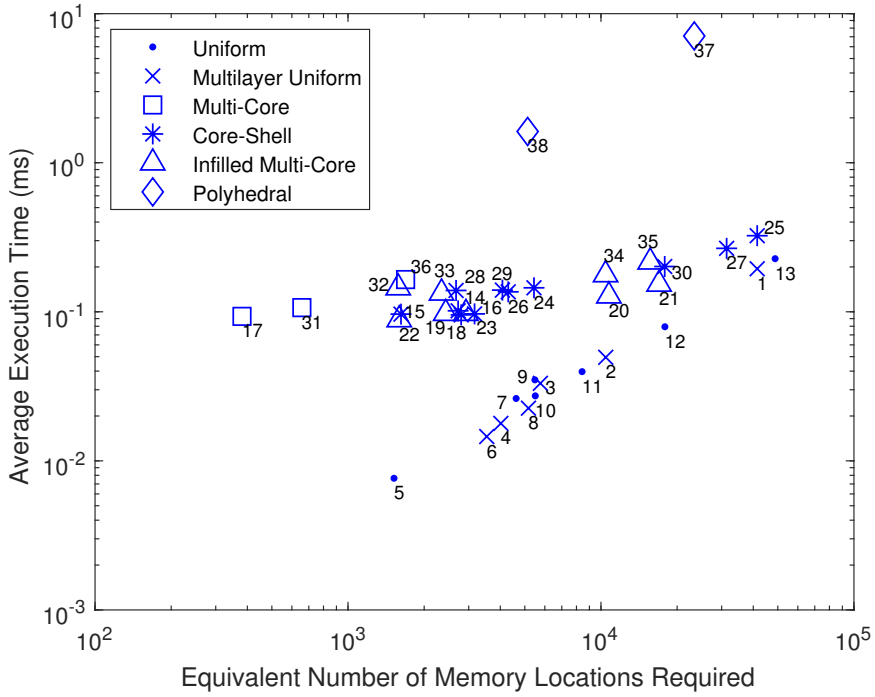

Figure 4: Average evaluation times as a function of memory requirements for the models examined.

Table 2: Performance Metrics for the Test Model Set

#	Packing Type	MultiMESH ID	η	$\overline{\tau}_{\text{eval}}$ (ms)	$\epsilon_{\text{RMS,low}}$ (m/s)	$\epsilon_{\text{RMS,high}}$ (m/s)
1	II	M76_00-60r0.059_M10286_60-90r0.016	41448	1.944	0.1779E-05	0.7315E-07
2	II	M111_00-60r0.053_M2500_60-90r0.025	10444	0.4950	0.4311E-05	0.2586E-06
3	II	M160_00-60r0.047_M1280_60-90r0.031	5760	0.3312	0.9452E-05	0.9402E-06
4	II	M248_00-60r0.041_M757_60-90r0.038	4020	0.1784	0.1573E-04	0.2279E-05
5	I	M884_00-85r0.038	3536	0.07644	0.3340E-03	0.4551E-04
6	II	M380_40-70r0.034	1520	0.1456	0.2995E-04	0.4994E-05
7	I	M1155_00-85r0.034	4620	0.2621	0.2032E-04	0.3041E-05
8	II	M1292_30-70r0.025	5168	0.2257	0.6019E-04	0.3458E-05
9	I	M1370_00-90r0.034	5480	0.3494	0.1495E-04	0.1959E-05
10	I	M1375_00-70r0.034	5500	0.2730	0.1050E-04	0.7099E-06
11	I	M2105_00-85r0.028	8420	0.3968	0.1644E-04	0.2031E-05
12	I	M4473_00-85r0.022	17892	0.7935	0.1039E-04	0.1194E-05
13	I	M12199_00-85r0.009	48796	2.271	0.5780E-05	0.5626E-06
14	IV	SH2_00-10_11.12_M620_10-70r0.034	2801	0.9537	0.2601E-04	0.4685E-05
15	IV	SH2_00-20_3.3_M395_20-60r0.034	1620	0.9646	0.3096E-03	0.1062E-03
16	IV	SH2_00-60_7.11_M737_60-85r0.034	3164	0.9683	0.2335E-04	0.3555E-05
17	III	SH2_00-70_12.13	381	0.9319	0.6448E-03	0.2536E-03
18	IV	SH2_00-70_12.13_M588_70-85r0.034	2725	1.016	0.2091E-04	0.3513E-05
19	V	SH2_12.12_CM522_00-70r0.031	2434	0.9755	0.1288E-03	0.3236E-04
20	V	SH2_10.10_CM2624_00-60r0.016	10746	1.278	0.2314E-03	0.7071E-04
21	V	SH2_12.12_CM4155_00-70r0.016	16966	1.532	0.8539E-04	0.2051E-04
22	V	SH2_10.10_CM336_00-60r.0031	1594	0.8845	0.3440E-03	0.1088E-03
23	V	SH2_17.18_CM558_00-60r0.034	2925	0.9755	0.1552E-02	0.1046E-03
24	IV	SH3_00-60_4.10.11_M1280_60-90r0.031	5434	1.449	0.9250E-05	0.9397E-06
25	IV	SH3_00-60_4.10.11_M10286_60-90r0.016	41458	3.238	0.1779E-05	0.7315E-07
26	IV	SH3_00-70_8.12.12_M964_70-90r0.031	4299	1.361	0.9218E-05	0.9287E-06
27	IV	SH3_00-70_8.12.12_M7735_70-90r0.016	31383	2.665	0.1780E-05	0.7315E-07
28	IV	SH3_00-70_8.12.13_M554_70-90r0.038	2674	1.391	0.1509E-04	0.2185E-05
29	IV	SH3_00-80_7.14.14_M885_80-95r0.031	4078	1.398	0.6224E-05	0.2632E-06
30	IV	SH3_00-80_7.14.14_M4331_80-90r0.016	17862	2.013	0.4474E-04	0.6852E-05
31	III	SH3_00-85_10.15.15	657	1.067	0.1347E-03	0.5590E-04
32	V	SH3_4.10.10_CM325_00-60r0.032	1579	1.449	0.3319E-03	0.1014E-03
33	V	SH3_8.12.12_CM478_00-70r0.032	2343	1.336	0.1028E-03	0.2365E-04
34	V	SH3_4.10.10_CM2537_00-60r0.016	10247	1.773	0.2314E-03	0.7069E-04
35	V	SH3_8.12.12_CM3804_00-70r0.016	15647	2.159	0.8347E-04	0.1968E-04
36	III	SH3_00-85_7.13.15	592	1.645	0.8135E-04	0.1834E-04
37	Poly	7790-facet, 3897-vertex polyhedral	23376	7.08	0.3540E-05	0.1084E-05
38	Poly	1708-facet, 856-vertex polyhedral	5130	1.62	0.4087E-04	0.1685E-04

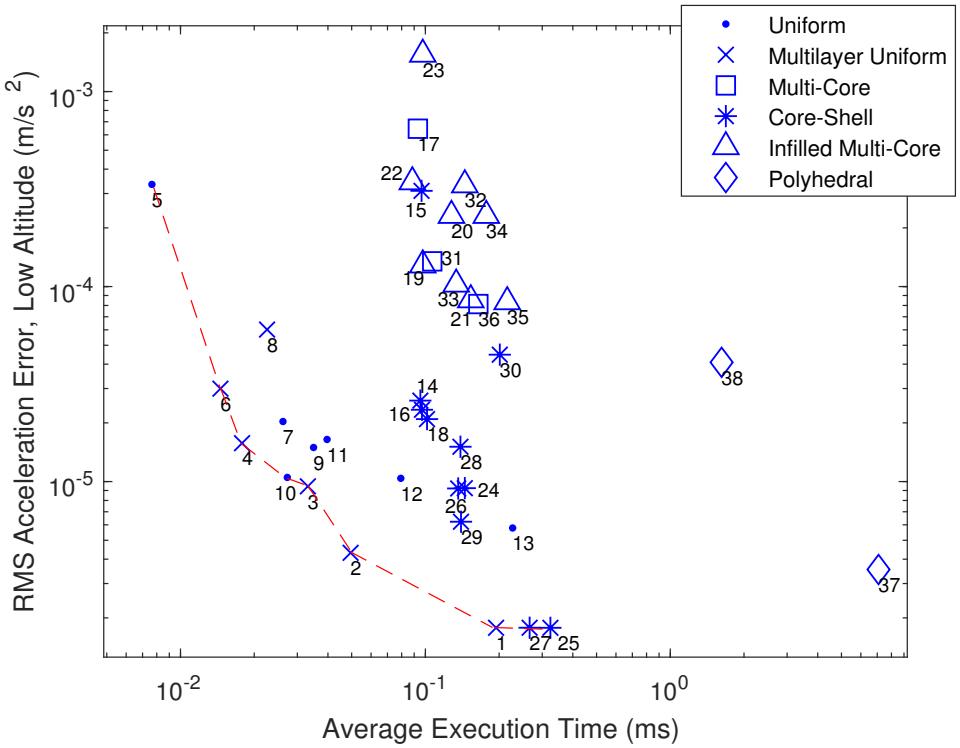

(a) Runtime

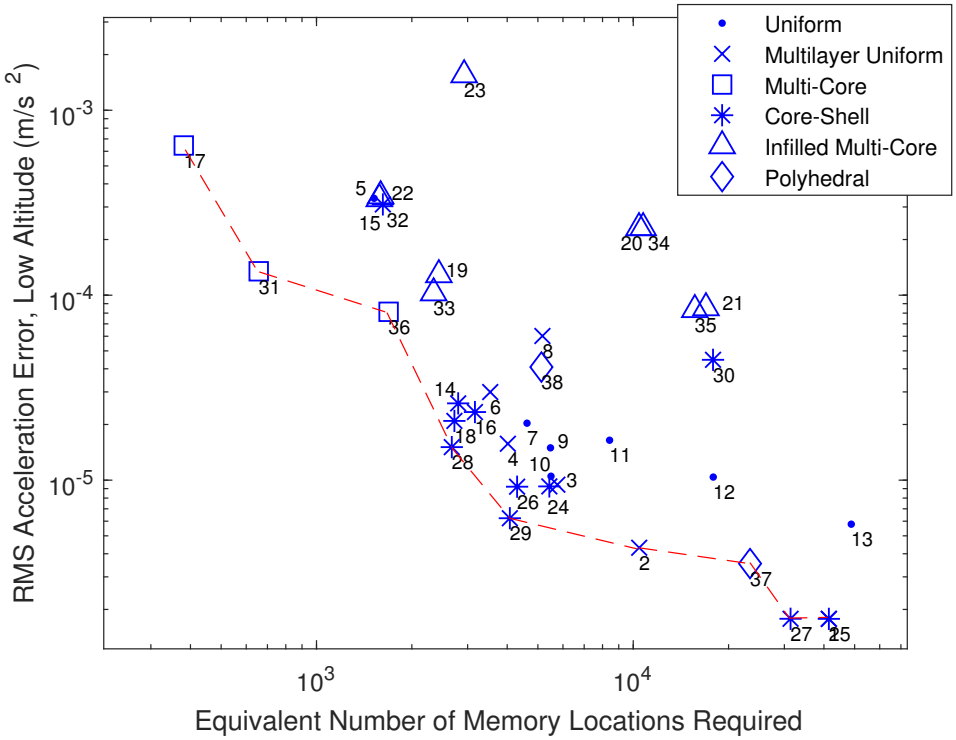

(b) Memory

Figure 5: Averaged low altitude (below 0.15625 R_a) RMS errors plotted against both average model evaluation time and memory requirements. Pareto frontiers are approximated with dotted lines.

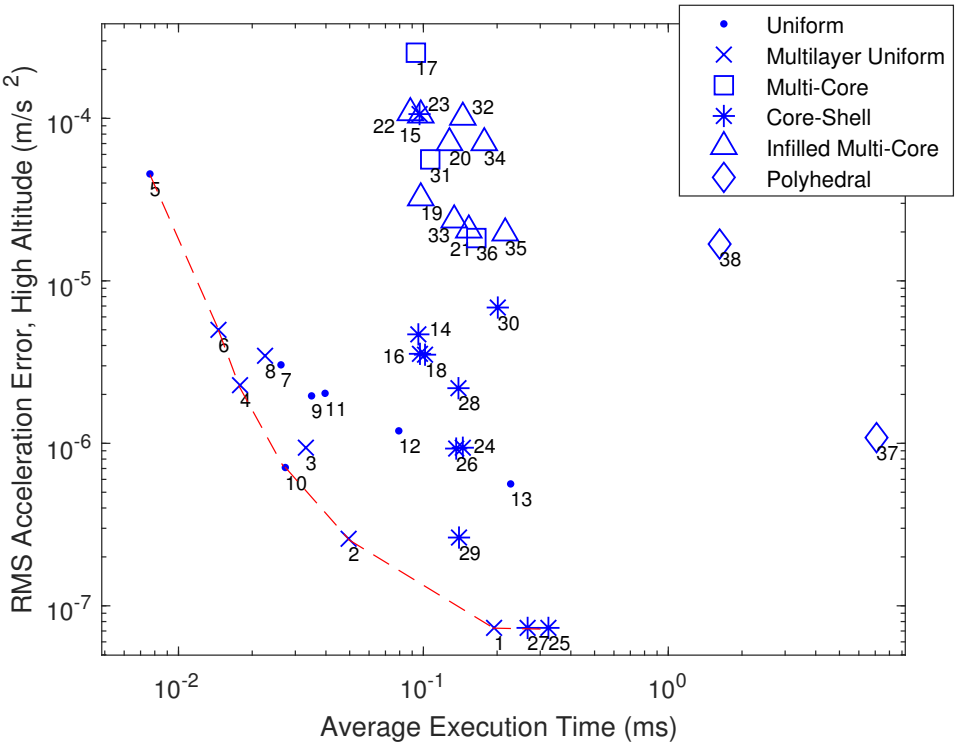

(a) Runtime

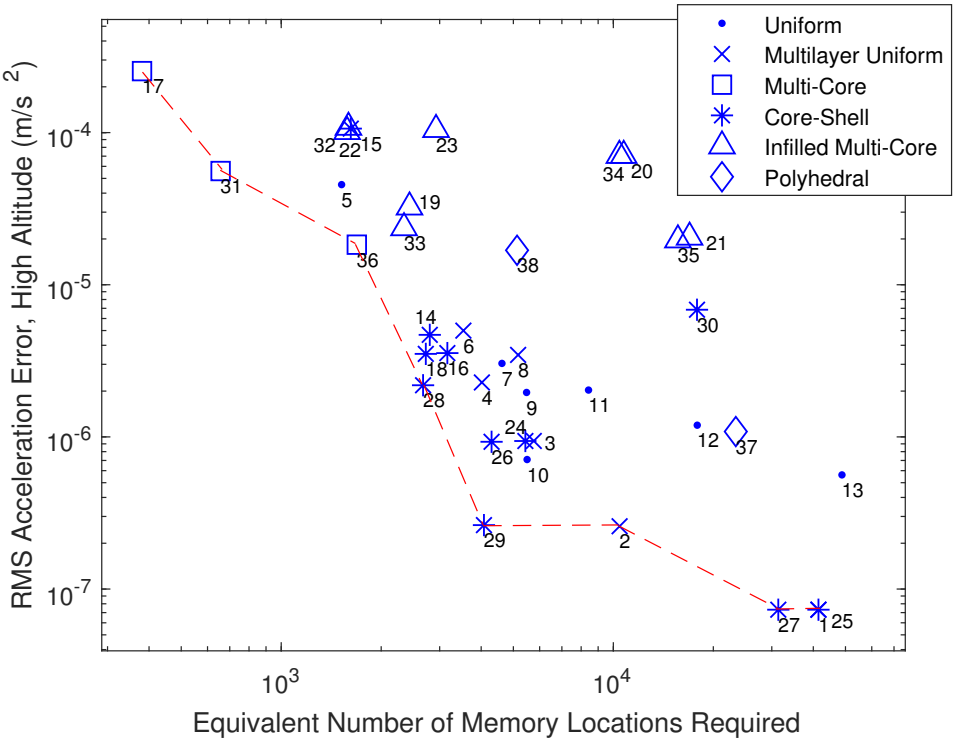

(b) Memory

Figure 6: Averaged high altitude (0.15625 R_a to 0.3125 R_a) RMS errors plotted against both average model evaluation time and memory requirements. Pareto frontiers are approximated with dotted lines.

In Figure 4, three primary groups of models can be observed. The first group, with the fastest runtimes, consists of Type I and II models which contain no spherical harmonics at all. The second group contains a mixture of Type III, IV, and V models, all of which incorporate two or more spherical harmonics elements. Despite the generally faster execution times, the first group's runtime required per memory unit increases more rapidly than that for the second group. This can be directly attributed to the relationship established in Eq. (19). While any increase in the number of mascons is scaled by 4 when calculating memory footprint, increases in the total number of spherical harmonics coefficients are scaled only by unity. Moreover, an efficient spherical harmonics code (such as the one implemented here) can mitigate the impact of added coefficients on execution speed as spherical harmonics fields increase in size. Mascons, on the other hand, have a fixed computational cost per element, regardless of how many are present. The third group contains only the reduced-resolution polyhedral models. Though their memory requirements may be similar to the MultiMESH models tested, calculating the gravitational potential using a polyhedral model requires summations over both the facets and the edges of the polyhedron. The necessity of establishing edge relationships between vertices and facets, then summing their gravitational influence decreases the efficiency of the polyhedron's memory footprint.

Since the primary goal of this work is to identify ways to place elements such that the number of elements is minimized while maintaining accuracy in the gravity field, the RMS error plots in Figures 5 and 6 are of particular interest. In these plots, the averaged errors of the MultiMESH models are plotted against the models' memory requirements and execution time. In this work, "optimal" designs are defined in the context of two-dimensional Pareto optimality; that is, optimal gravity models offer a combination of the two metrics being plotted such that no other models offer better performance on both of those metrics simultaneously. In other words, we seek models which fall as close to the lower left corner of the plots in Figures 5 and 6 as possible. The Pareto frontiers on these plots satisfy our search for optimal packing arrangements. It should be noted that these frontiers are unique to Eros; the Pareto frontiers for other bodies may suggest a different set of optimal model parameters. While the 2D Pareto frontiers discussed here remain useful when comparing the performance of the models tested, a wider exploration of the design space would enable a better definition of a three-dimensional Pareto front for all three performance metrics. Such an exploration will naturally follow this work.

In the plots of runtime versus error (Figs. 5a and 6a), several important features are present. First, the Pareto frontiers pass through several Type II (Multi-Layer Uniform) models for both altitude bins. At the low-error end of these frontiers, two Type IV models are also present (numbers 25 and 27). Type II models use their CPU time judiciously because they can bury fewer, larger mascons deep within the shape model, where local mass variations impact the surface field less. At the same time, Type II models allow an increase in element resolution at the near-surface layer, reducing surface field errors. The presence of the Type IV models at the tail end of the Pareto frontiers is unsurprising; models 25 and 27 both surround a core of 3 spherical harmonics elements with densely packed surface layers of small mascons. Given that the runtime Pareto frontiers are steeply sloped in Figure 5, these Type IV models represent an attractive optimal packing arrangement; for a small increase in runtime, one can obtain order-of-magnitude RMS error reductions over Type I (Uniform) models.

Examining the memory versus error plots (Figs. 5b and 6b), the benefits of including spherical harmonics elements are also clear. Type III and IV models are common along the Pareto frontiers, demonstrating the efficient use of memory space they offer. Of particular note are models 28 and 29; both of these Type IV models utilize a thin layer of medium-sized mascons to surround 3 spherical harmonics cores, and they both have comparable numbers of mascons and spherical harmonics coefficients. On the other hand, if a trajectory planner is primarily interested in a small model memory footprint, some Type III models may be a simple and attractive option for field representation. However, since surface accelerations at Eros are approximately $5mm/s^2$, the Type III models at the low-memory end of these Pareto frontiers would not be recommended for use in designing proximity operations, as their relative acceleration errors are approximately 10-20%.

Another notable feature present in all four plots in Figs. 5 and 6 is the relatively worse performance of the Type V (Infilled Multiple-Core) models on all fronts when compared to the somewhat similar Type III models. This suggests that burying any spherical harmonics elements beneath a layer of mascons helps to

reduce field errors induced by closeness of the spherical harmonics elements' surfaces to the shape model boundary (a common feature of Type V structures).[22]

Comparison Case

Table 3: Model Details for Comparison Case

Number	Type	Elements	Harmonic Coefficients	Field Sizes	Shape Model Scale
2	II	2611	0	N/A	60%,90%
29	IV	888	511	7x7,14x14,14x14	80%,90%

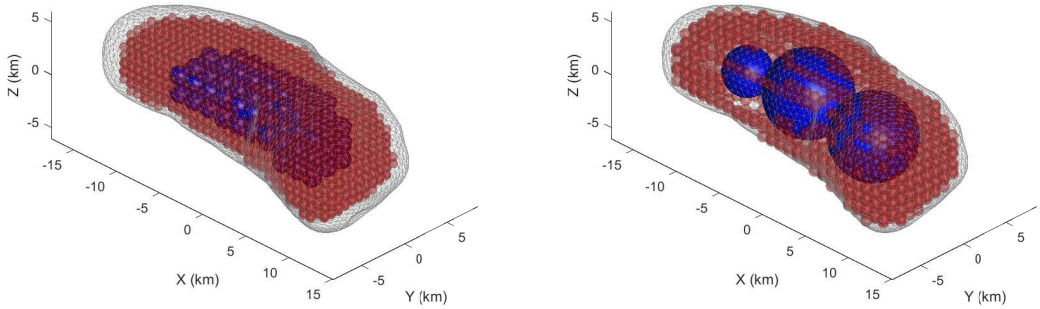

(a) M111_00-60r0.053_M2500_60-90r0.025

(b) SH3_00-80_7.14.14_M885_80-90r0.031

Figure 7: Packing structures for the example models 2 (a) and 29 (b) from Table 2.

To demonstrate the effects of adding spherical harmonics elements, two models are now compared. These two models are labeled "2" and "29" in Figures 5 and 6, and diagrams of their packing arrangments are shown in Figure 7, with details on the packing structure given in Table 3. Model 2 is packed with two layers of mascons, the innermost of which is filled with elements 1.7 km in diameter, and the outermost of which is filled with 800 m diameter elements. The inner layer falls within a 60% scale shape model, and the outer layer falls between the 60% scale shape model and a 90% scale shape model. Since only the the gravitational parameters are estimated, the nonlinear batch least-squares filter converges in one iteration. On the other hand, model 29 contains three large spherical harmonics elements within a 80% scale shape model, surrounded by a layer of smaller mascons between the 80% and 90% scale shape models. The nonlinear estimator converged in 6 iterations on a solution for the gravitational parameters and spherical harmonics coefficients for model 29.

Both models fall along at the high- and low-altitude memory Pareto fronts, and model 2 falls along the speed Pareto fronts as well (in fact, it is the only model tested that does). For its part, model 29 falls quite close to the speed Pareto fronts, and is one of the best-performing mid-sized core-shell models. As shown in Figure 8, the RMS and maximum errors for the two models are roughly similar across all altitudes, with model 2 performing slightly better near the surface. In the case of model 29, this accuracy comes at the cost of a longer evaluation time, while model 2 achieves the same by utilizing a large memory footprint.

CONCLUSION

In this work, mascon models have been revisited for the small body gravity problem with the intent to minimize the number of elements, optimize the placement of the elements, and maintain or increase the accuracy of the models. By introducing one or more spherical harmonics elements to the model and performing nonlinear batch least squares estimation of the model parameters, the design trade space for mascon models

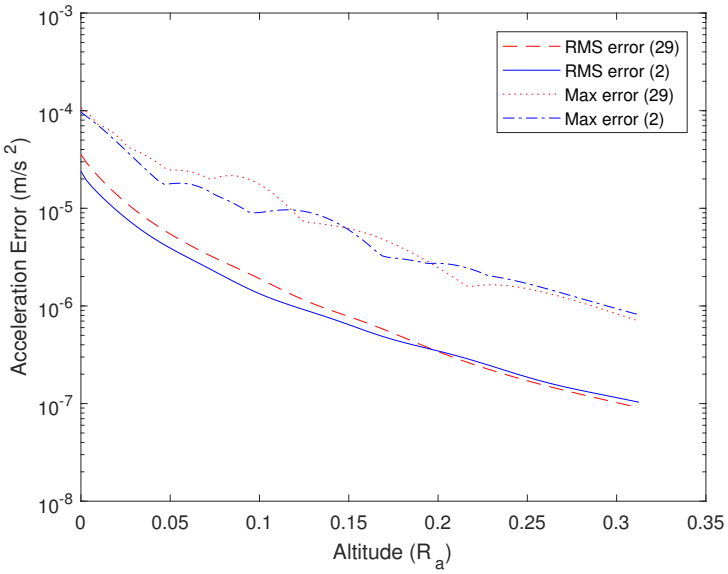

Figure 8: RMS and maximum error data as a function of altitude for comparison Models 2 and 29.

has been expanded. The evidence presented here suggests that using hybrid, mixed element mascon models with buried, small-to-midsize spherical harmonics fields can offer memory, accuracy, and computational speedup advantages over traditional discrete-element models. The hybrid models offer clear opportunities for parallelization; however, since individual spherical harmonics fields cannot typically be computed in parallel, keeping any spherical harmonics fields small is important to reduce any such losses. Such models help define a Pareto frontier in the gravity model design trade space. Models located along this frontier are expected to provide fast, accurate gravitational acceleration evaluations for the purpose of rapid trajectory design in the small body domain.

ACKNOWLEDGMENT

The work described in this paper was funded by NASA's Space Technology Mission Directorate through a NASA Space Technology Research Fellowship grant (NNX16AM59H). The authors thank Kenny Getzandanner at Goddard Space Flight Center for his input on this work and his support as the NASA Research Collaborator on the NSTRF grant.

REFERENCES

[1] J. Gal-Edd and A. Cheuvrant, "The OSIRIS-REx Asteroid Sample Return: Mission Operations Design," *SpaceOps 2014 Conference*, Washington, DC, AIAA, 2014.

[2] G. J. Whiffen, D. J. Grebow, and J. C. Smith, "Dawn's Mission to Ceres," *AIAA/AAS Astrodynamics Specialist Conference*, Washington, DC, AIAA, 2016.

[3] D. Y. Oh, D. Goebel, C. Polanskey, S. Snyder, G. Carr, S. M. Collins, G. Lantoine, D. Landau, L. Elkins-Tanton, P. Lord, and S. Tilley, "Psyche: Journey to a Metal World," *AIAA Propulsion and Energy Forum*, Washington, DC, AIAA, 2016.

[4] R. A. Werner and D. J. Scheeres, "Exterior Gravitation of a Polyhedron Derived and Compared with Harmonic and Mascon Gravitation Representations of Asteroid 4769 Castalia," *Celestial Mechanics and Dynamical Astronomy*, Vol. 65, No. 3, 1997, pp. 313–344.

[5] W. Kaula, *Theory of Satellite Geodesy: Applications of Satellites to Geodesy*. New York: Dover, 2000.

[6] G. Balmino, "Gravitational Potential Harmonics from the Shape of an Homogeneous Body," *Celestial Mechanics and Dynamical Astronomy*, Vol. 60, No. 3, 1994, pp. 331–364.

[7] R. A. Werner, "Spherical Harmonic Coefficients for the Potential of a Constant-Density Polyhedron," *Computers & Geosciences*, Vol. 23, No. 10, 1997, pp. 1071–1077.

[8] Y. Takahashi, D. J. Scheeres, and R. A. Werner, "Surface Gravity Fields for Asteroids and Comets," *Journal of Guidance, Control, and Dynamics*, Vol. 36, No. 2, 2013, pp. 362–374.

[9] S. Casotto and R. Casotto, "Cartesian Development of the Gravitational Potential Within the Hotine Sphere," *Advances in the Astronautical Sciences*, AAS, 2016.

[10] G. Romain and B. Jean-Pierre, "Ellipsoidal Harmonic Expansions of the Gravitational Potential: Theory and Application," *Celestial Mechanics and Dynamical Astronomy*, Vol. 79, No. 4, 2001, pp. 235–275.

[11] A. Colombi, A. N. Hirani, and B. F. Villac, "Adaptive Gravitational Force Representation for Fast Trajectory Propagation Near Small Bodies," *Journal of Guidance, Control, and Dynamics*, Vol. 31, No. 4, 2008, pp. 1041–1051.

[12] A. Colombi, A. N. Hirani, and B. F. Villac, "Structure Preserving Approximations of Conservative Forces for Application to Small-Body Dynamics," *Journal of Guidance, Control, and Dynamics*, Vol. 32, No. 6, 2009, pp. 1847–1858.

[13] N. Arora and R. P. Russell, "Efficient Interpolation of High-Fidelity Geopotentials," *Journal of Guidance, Control, and Dynamics*, Vol. 39, No. 1, 2016, pp. 128–143.

[14] K. R. Koch and F. Morrison, "A Simple Layer Model of the Geopotential from a Combination of Satellite and Gravity Data," *Journal of Geophysical Research*, Vol. 75, No. 8, 1970, pp. 1483–1492.

[15] K. R. Koch and B. U. Witte, "Earth's Gravity Field Represented by a Simple Layer Potential from Doppler Tracking of Satellites," *Journal of Geophysical Research*, Vol. 76, No. 35, 1971, pp. 8471–8479.

[16] H. J. Melosh, "Mascons and the Moon's Orientation," *Earth and Planetary Science Letters*, Vol. 25, No. 3, 1975, pp. 322–326.

[17] F. Morrison, "Algorithms for Computing the Geopotential Using a Simple Density Layer," *Journal of Geophysical Research*, Vol. 81, No. 26, 1976, pp. 4933–4936.

[18] W. L, G. Buechler, W. Downs, W. Sjogren, P. Muller, and P. Gottlieb, "A Surface-Layer Representation of the Lunar Gravitational Field," *Journal of Geophysical Research*, Vol. 76, No. 26, 1971, pp. 6220–6236.

[19] J. Palguta, J. D. Anderson, G. Schubert, and W. B. Moore, "Mass anomalies on Ganymede," *Icarus*, Vol. 180, No. 2, 2006, pp. 428–441.

[20] D. N. Weise, F. W. Landerer, and M. M. Watkins, "Quantifying and reducing leakage errors in the JPL RL05M GRACE mascon solution," *Water Resources Research*, Vol. 52, No. 9, 2016, pp. 7490–7502.

[21] H. Save, S. Bettadpur, and B. D. Tapley, "High-Resolution CSR GRACE RL05 mascons," *Journal of Geophysical Research: Solid Earth*, Vol. 121, No. 10, 2016, pp. 7547–7569.

[22] R. P. Russell and N. Arora, "Global Point Mascon Models for Simple, Accurate, and Parallel Geopotential Computation," *Journal of Guidance, Control, and Dynamics*, Vol. 35, No. 5, 2012, pp. 1568–1581.

[23] R. S. Park, R. A. Werner, and S. Bhaskaran, "Estimating Small-Body Gravity Field from Shape Model and Navigation Data," *Journal of Guidance, Control, and Dynamics*, Vol. 33, No. 1, 2010, pp. 212–221.

[24] S. Tardivel, "The Limits of the Mascons Approximation of the Homogeneous Polyhedron," *AIAA/AAS Astrodynamics Specialist Conference*, Washington, DC, AIAA, 2016.

[25] J. M. Pearl and D. L. Hitt, "Asteroid Gravitational Models Using Mascons Derived from Polyhedral Sources," *AIAA/AAS Astrodynamics Specialist Conference*, Washington, DC, AIAA, 2016.

[26] J. M. Pearl and D. L. Hitt, "Comparing the Computational Efficiency of Polyhedral and Mascon Gravity Models," *27th AIAA/AAS Spaceflight Mechanics Meeting*, AAS, 2017.

[27] J. M. Pearl and D. L. Hitt, "Asteroid Gravitational Models Using Surface Concentrations," *27th AIAA/AAS Spaceflight Mechanics Meeting*, AAS, 2017.

[28] S. Hesar, D. Scheeres, Y. Takahashi, J. McMahon, and A. French, "An Improved Method for Characterizing Small Body Density Distribution," *27th AIAA/AAS Spaceflight Mechanics Meeting*, AAS, 2017.

[29] S. J. Ostro, R. S. Hudson, M. C. Nolan, J.-L. Margot, D. J. Scheeres, D. B. Campbell, C. Magri, J. D. Giorgini, and D. K. Yeomans, "Radar Observations of Asteroid 216 Kleopatra," *Science*, Vol. 288, 2000, pp. 836–839.

[30] S. Pines, "Uniform Representation of the Gravitational Potential and Its Derivatives," *AIAA Journal*, Vol. 11, No. 11, 1973, pp. 1508–1511.

[31] D. A. Cicci, "Improving Gravity Field Determination in Ill-Conditioned Inverse Problems," *Computers & Geosciences*, Vol. 18, No. 5, 1992, pp. 509–516.

[32] O. Baur, "Tailored Least-Squares Solvers Implementation for High-Performance Gravity Field Research," *Computers & Geosciences*, Vol. 35, No. 3, 2009, pp. 548–556.

[33] B. Carcich, "MSI Optical Shape Models of 433 Eros," 2002.

View publication stats